Journal Pre-proof

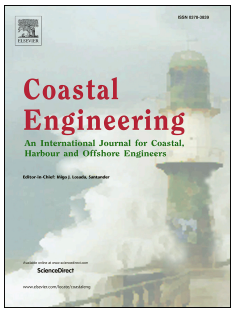

Using free satellite imagery to study the long-term evolution of intertidal bar systems

Xiaodong Zhang, Chuang Wu, Yongchang Zhang, Rijun Hu, Zuosheng Yang

PII: S0378-3839(22)00040-0

DOI: https://doi.org/10.1016/j.coastaleng.2022.104123

Reference: CENG 104123

To appear in: *Coastal Engineering*

Received Date: 27 September 2021

Revised Date: 30 January 2022

Accepted Date: 25 March 2022

Please cite this article as: Zhang, X., Wu, C., Zhang, Y., Hu, R., Yang, Z., Using free satellite imagery to study the long-term evolution of intertidal bar systems, *Coastal Engineering* (2022), doi: https://doi.org/10.1016/j.coastaleng.2022.104123.

Zhang Xiaodong: Conceptualization, Methodology, Software, Data curation, Writing-Original draft preparation, Writing-Reviewing and Editing, Funding acquisition. **Wu Chuang**: Visualization, Investigation. **Zhang Yongchang:** Formal analysis, Writing-Reviewing and Editing. **Hu Rijun**: Conceptualization, Writing-Review & Editing, Funding acquisition. **Yang Zuosheng:** Writing-Reviewing and Editing.

Using free satellite imagery to study the long-term evolution of intertidal bar systems

Xiaodong Zhang[1*], Chuang Wu[1], Yongchang Zhang[2], Rijun Hu[1], Zuosheng Yang[1]

[1]Key Lab of Submarine Geosciences and Prospecting Techniques, MOE and College of Marine Geosciences, Ocean University of China, Qingdao 266100, China

[2]School of Management, University of Science and Technology of China, Hefei 230026, China

* Correspondence to: Xiaodong Zhang, zxd@ouc.edu.cn

Abstract

Intertidal bar systems (IBSs) are ubiquitous geomorphic features on beaches and play an important role in nourishing and protecting beaches. IBSs can also pose a significant threat to nearshore swimmers and ships. Therefore, studying the evolution of IBSs will yield valuable insight in understanding the dynamic nature of beaches, provide help in protecting beaches from current widespread erosion, and provide early warning of potential hazards. However, the data used by previous approaches are commonly site-specific and labor-intensive (or expensive), which restricts their application.

This paper introduces a new approach for studying the long-term evolution of IBSs based on free satellite imagery. This satellite approach uses three methods, namely bar, trough, and breaker methods, to directly recognize the planar positions of IBSs. This approach has low requirements on satellite images, therefore it is conducive to making full use of the precious historical satellite images to study the highly dynamic evolution of IBSs in recent decades, which cannot be measured and photographed again. Based on the terabytes of free satellite imagery, this approach can be used on almost all beaches in the world, which will greatly expand the study object pool and facilitate the selection of study

objects in different types of marine conditions.

This paper also introduces how to use the satellite approach based on a case study. The case study quantitatively revealed the forming, migration, decay, and distribution of the IBSs around the Feng River mouth in China, evaluated the errors of the satellite-derived position and migration rate, analyzed the main factors affecting their evolution, and discussed the main factors influencing their evolution and their influence on the evolution of adjacent beaches.

Keywords

Satellite image; Intertidal bar system; Bar and trough; Ridge and runnel; Beach evolution; River mouth

1. Introduction

An intertidal bar system (IBS) is comprised of an intertidal bar and its shoreward trough located between mean low and high spring water levels (Kroon and Masselink, 2002; Anthony et al., 2005; Masselink et al., 2006; Biausque et al., 2020). IBS was also named “ridge and runnel” (King and Williams, 1949). Owing to the term “ridge and runnel” being ambiguous (Biausque et al., 2020), this paper uses the more popular “IBS” following the recent literature list above.

IBSs are ubiquitous features on meso- and macro-tidal beaches (Kroon and Masselink, 2002; Masselink et al., 2006; Biausque et al., 2020), and they are also found on micro-tidal beaches (Guedes et al., 2011a; Cheng and Wang, 2018). IBSs play an important role in protecting and nourishing beaches by reducing wave energy and providing sand supply (Masselink et al., 2006; Sassa and Watabe, 2009; Gijsman et al., 2019; Biausque et al., 2020). IBSs can also induce rip currents, which pose a significant threat to nearshore swimmers (Stive and Reniers, 2003; Scott et al., 2011; Caldwell et al., 2013). Estuarine IBSs can also threaten ships trying to enter (or leave) estuaries (Harrison, 2015). Therefore, studying the evolution of IBSs will yield valuable insight in understanding the dynamic

nature of beaches, provide important references for the design of environment-friendly coastal engineering and beach nourishing measures, and provide early warnings of potential hazards (Hoefel and Elgar, 2003; Sassa and Watabe, 2009; Bouvier et al., 2017; Radermacher et al., 2018; Kuang et al., 2019a). Under the current circumstance of widespread beach erosion and increasing intimacy between humans and beaches (Nicholls and Cazenave, 2010; Alexandrakis et al., 2015; Luijendijk et al., 2018; Jackson and Nordstrom, 2020; Vousdoukas et al., 2020), such researches are necessary and urgent.

Previous researches mainly use field-survey profile data (e.g., King and Williams, 1949; Masselink and Anthony, 2001; Kroon and Masselink, 2002; van Houwelingen et al., 2006; Kuriyama et al., 2008; Quartel et al., 2008; Di Leonardo and Ruggiero, 2015; Cheng and Wang, 2018), aerial photographs (e.g., Masselink and Anthony, 2001; Kroon and Masselink, 2002; Moore et al., 2003; van Houwelingen et al., 2006; Aleman et al., 2017), LiDAR (light detection and ranging) data (e.g., Anthony et al., 2005; van Houwelingen et al., 2006; Reichmüth and Anthony, 2007; Aleman et al., 2017; Miles et al., 2019), and Argus (shore-based video system) images (e.g., van Enckevort and Ruessink, 2001; Stive and Reniers, 2003; Holman and Stanley, 2007; Quartel et al., 2007, 2008; Ribas et al., 2010; van de Lageweg et al., 2013; Harrison et al., 2017; Bouvier et al., 2017; Phillips et al., 2017) to study the evolution of IBSs. Diverse conceptual and numerical models have also been designed to understand the past and predict the future evolution of IBSs (e.g., Wright and Short, 1984; Hoefel and Elgar, 2003; Masselink, 2004; Quartel et al., 2008; Sassa and Watabe, 2009; Cohn and Ruggiero, 2016).

One-dimensional field-survey profile data are detailed and accurate, and related researches laid a solid foundation for understanding the evolution of IBSs. However, field surveys are labor-intensive and time-consuming, and the beach surveys can only be performed during the short (less than 2 hours) time windows before and after the low spring tides. These factors limit the spatial-temporal range and interval of the field-survey data, resulting in the long-term and continuous IBS data being relatively scarce (Masselink et al., 2006; Di Leonardo and Ruggiero, 2015). Planar aerial photographs, Argus images, and

LiDAR data save manpower and can be used to study the evolution of lBSs in two dimensions. However, these data are also site-specific just like the field-survey data. Moreover, these data are expensive, which in turn restricts their application. In summary, related researches mainly focused on a limited number of beaches, while more beaches, especially the beaches in developing and undeveloped countries, were rarely studied.

Although great advances have been achieved, admittedly, our understanding of the IBSs in terms of their forming, migration, decay, distribution, and the factors influencing their evolution, remains limited (Masselink et al., 2006; Di Leonardo and Ruggiero, 2015; Biausque et al., 2020). The reasons might be mainly attributed to the highly dynamic and complex nature of the IBSs and the limited data just mentioned (Stive and Reniers, 2003; Reichmüth and Anthony, 2007; Di Leonardo and Ruggiero, 2015; Biausque et al., 2020). Due to the limited data too, previous models are mostly of short time-scales and site-specific (Masselink and Anthony, 2001; Stive and Reniers, 2003; Fernández-Mora et al., 2015; Cheng and Wang, 2018), and more data will be necessary to build future general models (Biausque et al., 2020).

In recent decades, satellites regularly observed most of the earth's surface from the zenith, and satellite imagery offers a unique opportunity to study the long-term evolution of IBSs around the world, which cannot be measured and photographed again (Lafon et al., 2004; Bergsma et al., 2019; Román-Rivera and Ellis, 2019). Lafon et al. (2004), van Dongeren et al. (2008), Holman et al. (2013), Bergsma et al. (2019), and Najar et al. (2021) invert the elevation (or water depth) of IBSs using satellite image’s digital number or image difference between satellite bands originated from their tiny time delays. Although these approaches are promising with the progress of technology, their applications are limited at present because the methods of using planar image inverting vertical elevation are indirect and complicated. The inversions are significantly affected by atmospheric correction, water turbidity, wave conditions, etc. As a result, the inversion errors are notoriously large (a few meters in vertical) (Román-Rivera and Ellis, 2019; Najar et al., 2021).

Lippmann and Holman (1990), van Enckevort and Ruessink (2001), Stive and Reniers (2003), Ribas et al. (2010), Guedes et al. (2011b), and Phillips et al. (2017) estimate the

cross-shore position of nearshore bar crest through the identification of the high-intensity area in the Argus images. However, the methods mainly use time-averaged images during a short period (e.g., 10 minutes), and most satellites cannot provide such images. Quartel et al. (2007) delineate the landward boundaries of the intertidal bar and trough on classified Argus images, providing a practical method of studying the IBSs based on planar images.

Although satellite images have been widely used to recognize beach shorelines (e.g., Luijendijk et al., 2018; Vousdoukas et al., 2020; Zhang et al., 2021a) and recent reviews have highlighted their promise in the study of IBSs (Román-Rivera and Ellis, 2019; Biausque et al., 2020), related studies are surprisingly scarce. The reasons might be partly attributed to that previous shoreline recognition methods mainly focused on automatic recognition algorithms, and therefore, the methods are unable to efficiently process the satellite images with complex beach geomorphic features such as the IBSs (Zhang et al., 2021a).

Recently, Zhang et al. (2021a) provide a computer-aided shoreline position recognition software (CASPRS) to directly recognize the shoreline positions on beach transects. Based on the subpixel shoreline position recognition, human-computer interaction, and transect-focused technologies, the software is expected to effectively recognize the complex beach geomorphic features from satellite imagery. Using the early version of the software, Zhang et al. (2020, 2021b) have studied the long-term evolution of river mouth bars in the Changjiang River mouth.

Using the latest version (version 2.1) of the CASPRS software, this paper presents a new satellite approach to study the long-term evolution of IBSs. This paper first introduces the theory and method of the approach, and then introduces its application taking the Feng River mouth as an example. In addition, the systematic and random errors are also evaluated using field-survey data and statistical methods.

2. Study area

The Feng River is a small, mountainous river in coastal Qingdao, with a length of 35 km and a watershed area of 303 km^2 (Fig. 1). The river flows into the Lingshan Bay and

provides an important source of sand for the formation of Lingnan Beach (Cui and Li, 1987). Before the 1950s, the Feng River was a seasonal river with abundant water in summer and autumn but basically cut off in winter and spring, and it was also called "crazy river" or "evil river" by local people because of its frequent floods. Later, the river was relieved of the flood disaster after a series of regulations, especially the construction of the Tieshan Reservoir in the upper reaches from 1957–1967. Now, the Feng River basin has been urbanized and merged into the Qingdao High-tech Zone, a state-level economic development zone.

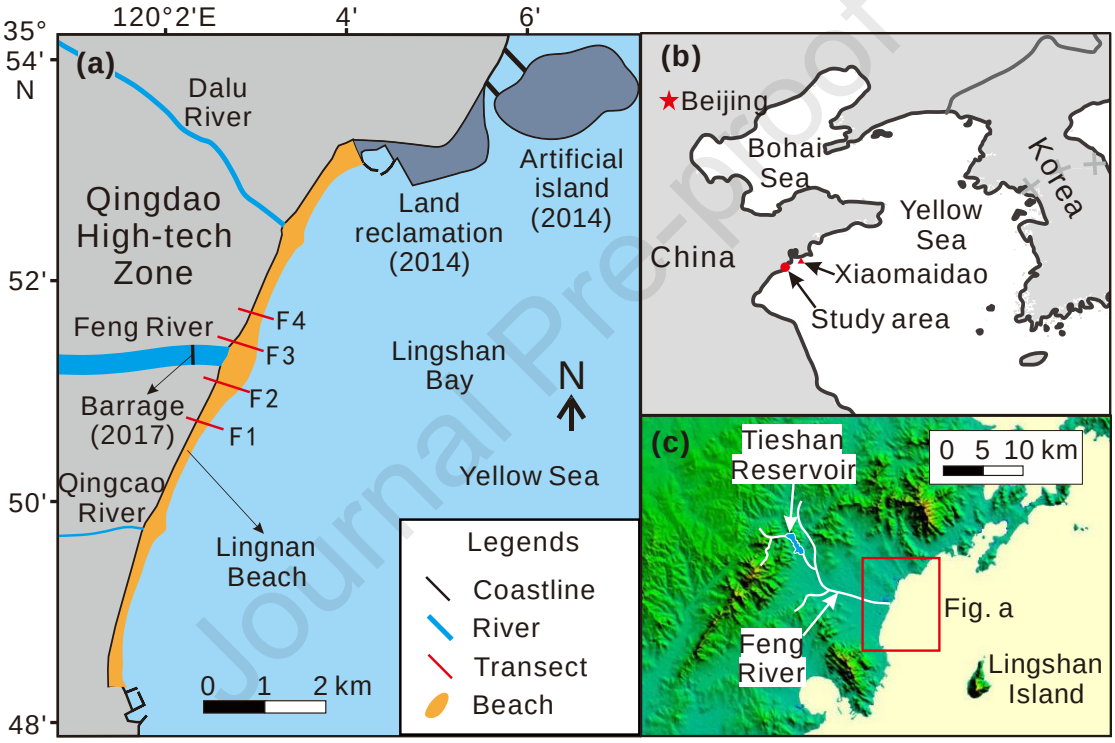

Fig. 1 The Feng River mouth and Lingnan Beach (a), their surrounding topography (b), and their location in China (c). Fig. a was mainly depicted from the Sentinel image of 2021/3/12 (Supplemental Fig. 1) when the tidal height was –2.03 m (relative to mean sea level).

Many barrages, including the barrage built in 2017 and 400 m from the river mouth (Fig. 1a, Supplemental Fig. 1), have been built along the river since the 1960s. As a result, the water discharged into the sea has decreased significantly (Bian et al., 2019). According to the measured data of local hydrological station (Qingdao Water Resources Bulletin

2017–2019), the water discharged into the sea was averaged of 2.4 M m^3/year and only 2% of the natural runoff, and the sediment discharged into the sea has been cut off due to the barrier effect of the barrages. In turn, the river channel close to the river mouth has been silted up by marine sediment inputs (Kuang et al., 2019b).

Lingnan Beach is a slightly concaved beach with bulges around local river mouths, of which the bulge around the Feng River mouth is the largest (Fig. 1a). The beach is mainly composed of well-sorted (sorting coefficient is 0.38–0.83) and fine-medium (median size is 1.2–2.6Φ) sand (Xu et al., 2014). In 2014, for the development of the Qingdao High-tech Zone, the northern headland of Lingnan Beach was enclosed, and further north, a large artificial island was built (Fig. 1).

The local tides are typical semidiurnal with a meso-tidal range. The mean high and low waters are 1.38 and –1.40 m, the highest high and lowest low waters are 2.94 and –3.12 m, the mean and mean spring tidal ranges are 2.78 and 4.75 m, respectively. The nearshore tidal currents flow back and forth along the coast, rising to the southwest and falling to the northeast; the tidal currents in the Feng River channel flow along the river channel, rising to the west and falling to the east, and the maximum tidal current velocity is 0.3~1.0 m/s. The tidal currents around the Feng River mouth are in a transitional state between the above two states (Kuang et al., 2019b).

According to the measured wave data of Xiaomaidao hydrological station (41 km to the study area), the local waves are weak with a mean $H_{1/10}$ (average wave height of the highest 1/10 waves) of 0.76 m, and the probabilities of $H_{1/10}$ being less than 0.5 and 1.0 m reach 57% and 88%, respectively. According to the ratio between the mean tidal range and mean wave height, the study area is tide-dominated (Hayes, 1979; Cui and Xia, 1992). The waves mainly come from the southeast, roughly perpendicular to the local shoreline. The total frequency of waves from east-south-east, south-east, and south-south-east reaches 47%.

3. Data and methods

3.1. Data source and preprocessing of satellite images

816 satellite images of the study area from 1984 to 2021 were used (Fig. 2). The dataset was downloaded from Google Earth Engine (https://earthengine.google.com/) using a JavaScript program: "GEEdownloader" (https://github.com/ouczxd/CASPRS). All the Landsat TM, ETM+, and OLI images, and the Sentinel MSI images of the study area with cloud cover less than 80% were downloaded. The resolutions of the Landsat and Sentinel images are 30 and 10 m, respectively. For consistency, the resolution of Landsat images was improved to 10 m using the bicubic interpolation method. The images were synthesized by the near-infrared, red, and green bands, and then stretched using a Python program: "ImageConverter" (https://github.com/ouczxd/CASPRS) according to the frequency distribution of each image's digital values for better visual effect.

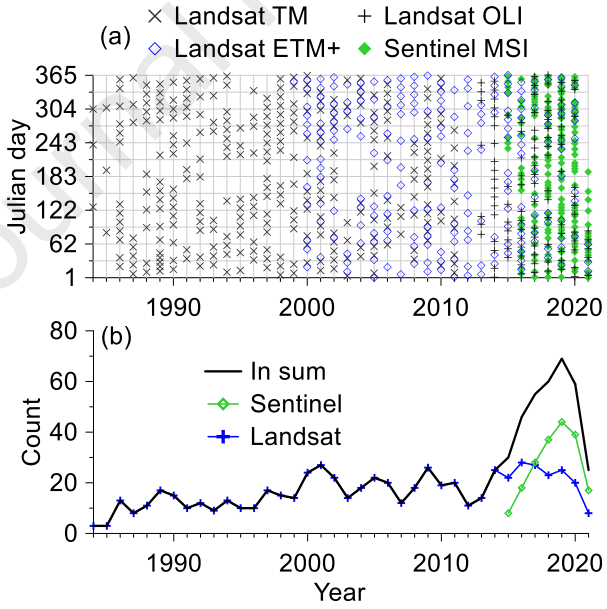

Fig. 2 The shooting time, sensor type (a), and annual count (b) of the Landsat and Sentinel images of the Feng River mouth from 1984 to 2021

In the processed false-color images, the dry beach is bright-white, the wet beach is brown, the breaker is blue-white, the water is blue, and the vegetation is red (Fig. 3, Supplemental Fig. 1 and 2). Blurry images were removed manually, leaving 816 good

images. The good images before 2015 are all Landsat images, 10–20 per year. Since the launch of the Sentinel satellite in 2015, the number of good images has increased dramatically, and the total numbers were as high as 60–70 per year in 2018–2020.

3.2. Recognition methods of IBSs

When the instantaneous water level is between the bar crest and trough bottom, the bar method is used to recognize the position of IBS on the transect. Bar's landward waterline is recorded as the dividing line between bar and trough (hereinafter referred to as dividing line), and bar's seaward waterline is the literal meaning (Fig. 3a and 4). When the instantaneous water level is lower than the trough bottom, the bar and beach are connected in the satellite image. However, the trough is wet and therefore dark relative to the adjacent bar and beach, or the trough is blue when enough water is retained in the trough. In this condition, the trough method is used, and the dividing line position is recognized according to the color change along the transect (Fig. 3b and 4). When the instantaneous water level is greater than the bar crest, a breaker will be found on the bar crest and its seaward slope when the waves are strong enough. In this condition, the breaker method is used, and the breaker's landward boundary line is recognized as the dividing line (Fig. 3c and 4).

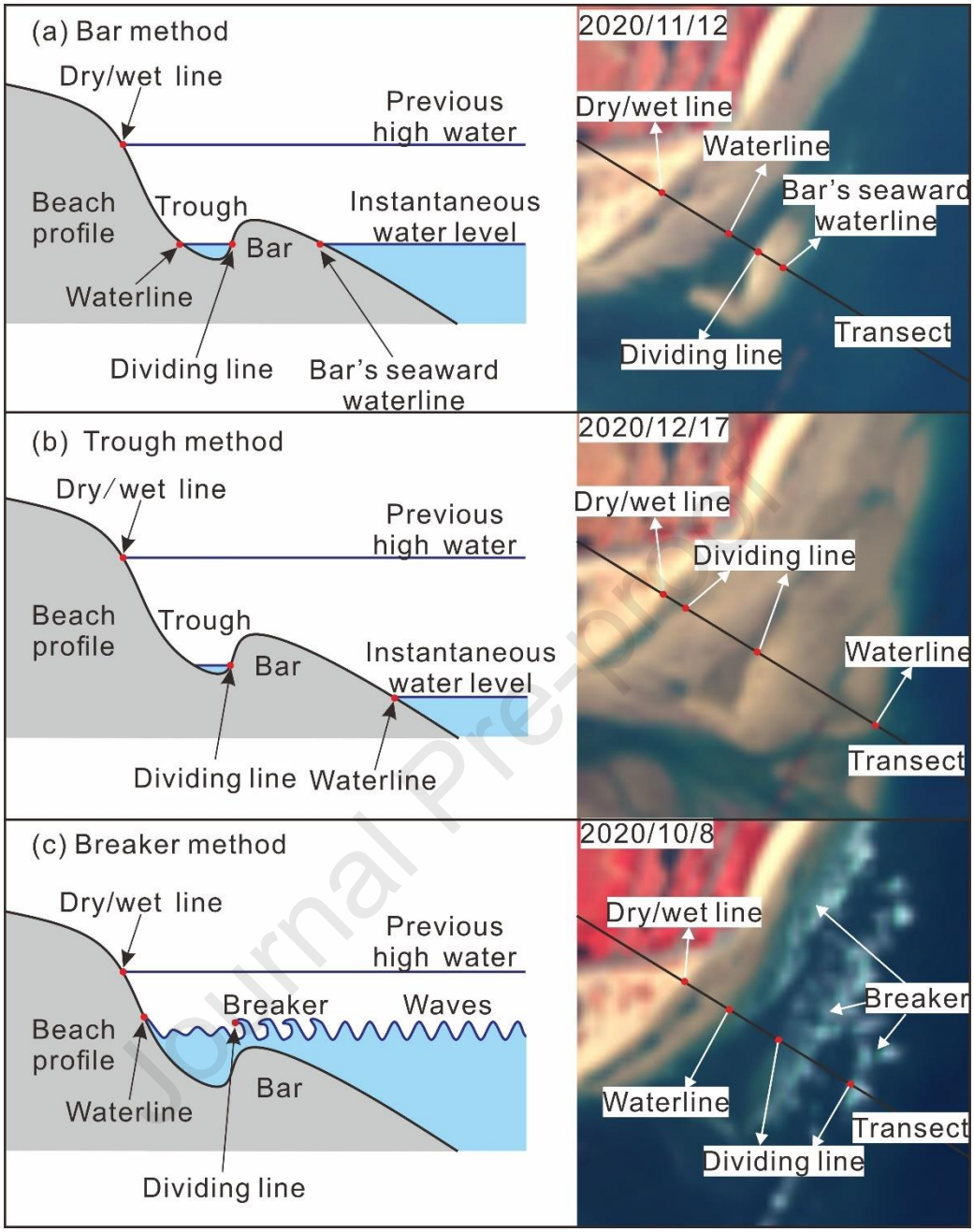

Fig. 3 Three recognition methods of IBSs: (a) bar method when the instantaneous water level is between the bar crest and trough bottom, (b) trough method when the instantaneous water level is lower than the trough bottom, and (c) breaker method when the instantaneous water level is greater than the bar crest

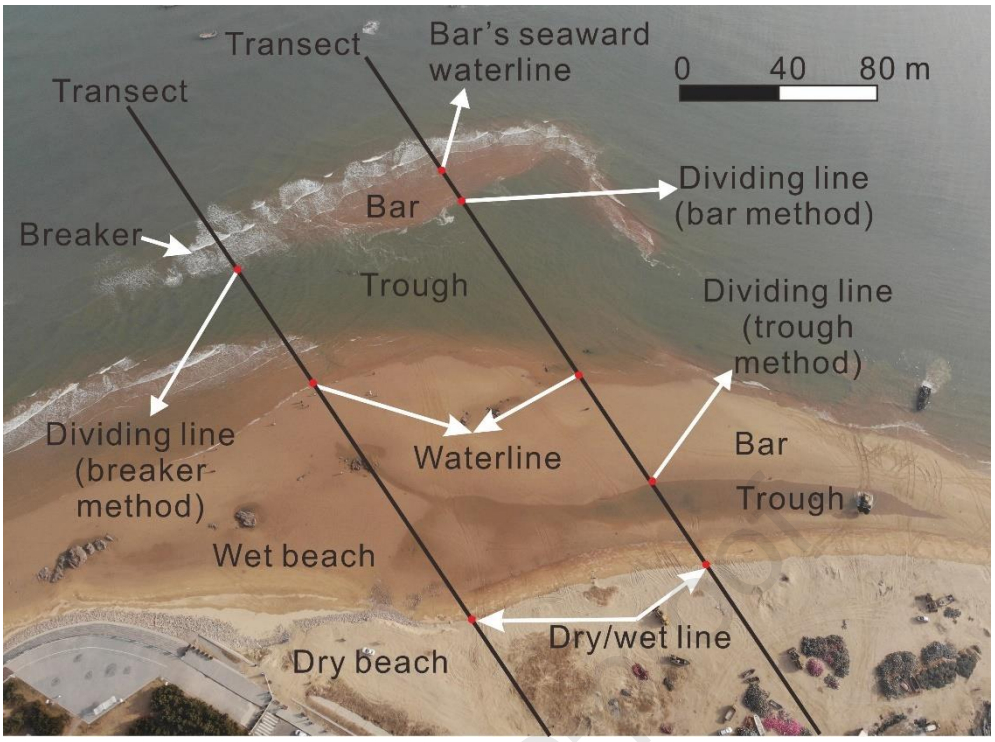

Fig. 4 Drone image of the northeast bank of the Feng River mouth taken at an altitude of 300 m at 14:55 2021/1/13. The tidal height was 0.31 m (relative to mean sea level). The IBSs are the same IBSs shown in Fig. 3a. The top bar was partly drowned, and its left part was covered by a breaker.

Except for the above two position indicators of IBS, the dry/wet line (the line between the bright dry beach and brown wet beach) and waterline (the line between the brown wet beach and blue water) positions of beach were also recognized after Zhang et al. (2021a) (Fig. 3, 4). When the instantaneous water level is lower than the trough bottom, the relevant bar's seaward waterline is recognized as the waterline of beach as the bar and beach are connected (Fig. 3b, 4).

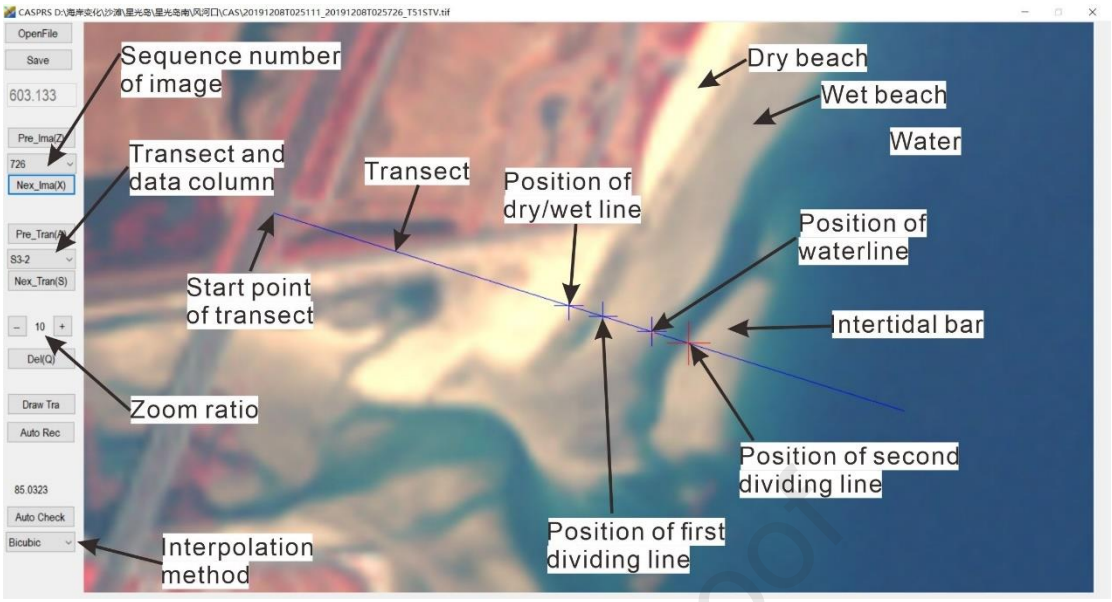

Fig. 5 Operation interface of the computer-aided shoreline position recognition software: CASPRS

The transect-focused CASPRS software was used to recognize the abovementioned four position indicators on four study transects F1–4 (Fig. 1, 5). For the transects F1 and F4, four data columns were used to record the four position indicators on each transect, respectively. However, for the transects F2 and F3, owing to multiple IBSs often appearing at the same time, an extra data column was added to record the dividing line positions respectively. In all, there are 18 data columns.

The dry/wet line and waterline positions were firstly auto-recognized and then manually revised. However, the dividing line positions were recognized manually as their auto-recognition algorithm has not yet been developed. All the recognition work could be completed within 2 days.

3.2. Processing of the position data

The dividing line positions on each transect were grouped manually according to their proximity relation and change trends (Fig. 6), and the planar shapes of the IBSs were also referenced when they were difficult to be grouped (Supplemental Fig.3). The onshore migration rate of IBS was calculated through the regression analysis of the dividing line positions versus time. The reason for using the dividing line positions instead of the bar's

seaward waterline positions is because the data amount of the latter is significantly smaller than that of the former and its fluctuation is relatively large, as shown below. The elevation of IBS, more precisely the elevation of the dividing line position, was estimated according to the dividing line position and the best-fit function of the profile shape. The profile shapes were measured using RTK-GPS in 2021/4/27–28, and the best-fit functions were calculated using the second-order polynomial fitting method (Masselink and Anthony, 2001).

The RTK-GPS survey paths were along the transects and from the coastal engineering to the instantaneous waterline of the beach at the measurement time (within 1 hour before and after the low spring tide). The measuring points are 1–10 m apart, which depends on the slope of the beach profile. The planimetric and altimetric accuracies of the RTK-GPS data are all less than 0.03 m.

The position data and the water level data were projected on the beach profile graph for an intuitional comparison. The water level data, including the instantaneous water levels when the satellite images were taken and the previous high-water levels before the satellite images were taken, were calculated by NAO.99b, a tide simulation model provided by Matsumoto et al. (2000). The simulated water level data were further corrected using the seasonal sea-level deviation in the study area (Zhang et al., 2018; 2021a). The comparison with the measured water level shows that the mean absolute error of the corrected simulated water level data is 0.14 m.

3.3. Error assessment

The systematic and random errors of the satellite-derived dividing line position were evaluated using field-survey data and statistical methods. For the evaluation of the systematic errors, the satellite-derived dividing line positions closest to the RTK-GPS survey time were compared with the RTK-GPS data. Owing to the rapid migration of the IBSs, the satellite-derived dividing line positions were corrected according to their onshore migration rates and the time delays between the field survey and the satellite images. The random errors were evaluated based on the standard deviations of the residuals of the

dividing line positions, and the residuals were derived from the regression analysis when calculating the onshore migration rates. The residuals of the dividing line positions were further used to evaluate the systematic errors of the three recognition methods.

The relative and absolute errors of the onshore migration rate were calculated according to Equations 1 and 2, respectively.

$$\text{Relative error} = \sqrt{\frac{\frac{1}{R^2}-1}{n-2}} \quad (1)$$

$$\text{Absolute error} = \text{Relative error} * |\text{Onshore migration rate}| \quad (2)$$

In which, R^2 is the determination coefficient of the regression analysis used to calculate the onshore migration rate, and n is the total number of the data pairs used to calculate the onshore migration rate.

4. Results

4.1. Position changes of the IBSs

Fig. 6 shows the position changes of the IBSs around the Feng River mouth on the transects F1–4 from 1984 to 2021. Fig. 6 also shows the dry/wet line and waterline positions of Lingnan Beach, which were stable in the long term but seriously affected by the onshore migrations of the IBSs. The IBSs were numbered generally according to their forming time, and the sequence number of zero was used to indicate the IBSs located stably at the mean low water.

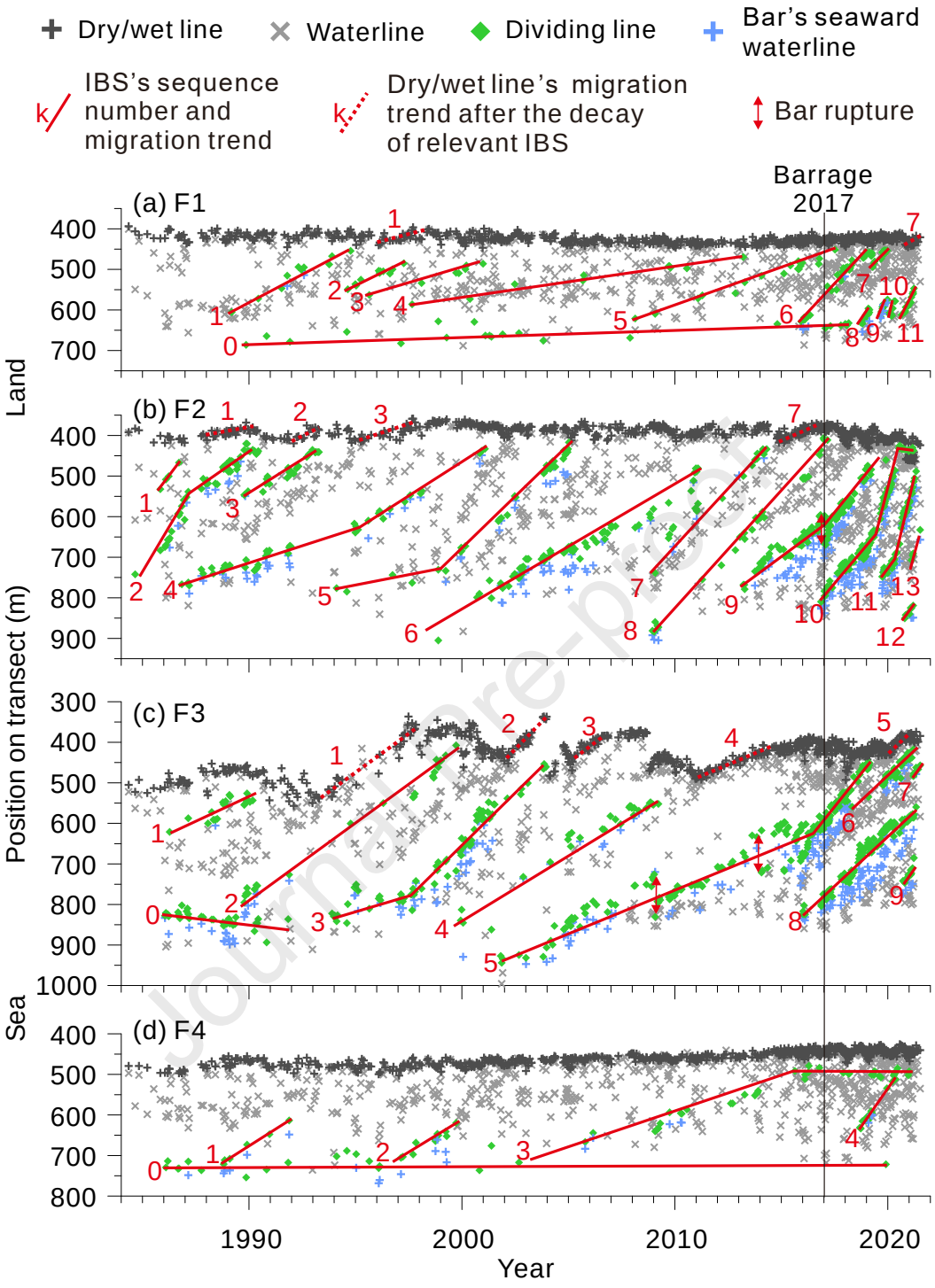

Fig. 6 Position changes of the IBSs around the Feng River mouth on the study transects F1 (a), F2 (b), F3 (c), and F4 (d) from 1984 to 2021

Except for the No.0 IBSs, the other IBSs migrated onshore linearly. Most IBSs migrated onshore at constant rates, some migrated onshore in stages with accelerated rates, such as F2*4, and only the onshore migrations of F2*2, F2*10, and F4*3 slowed

down. The bar crests of F2*9 and F3*5 ruptured (or abrupt seaward and landward shift, Quartel et al. (2007) also named the phenomenon as bar's morphological reset) when they migrated onshore. The decay or welding with the beach of some IBSs, such as F1*1, had triggered the onshore migration of dry/wet line positions.

The changes of the bar's seaward waterline positions were like that of the corresponding dividing line positions. However, the fluctuation ranges of the former are relatively large, which should be mainly attributed to the bar's seaward slope being gentle than its landward slope. The data amount of the bar's seaward waterline positions is 535 in total, only 38% of the dividing line positions, which should be attributed the former can only be recognized by the bar method, while the latter can be recognized by three methods.

The onshore migration rates varied between –10~199 m/year, negative value means offshore migration (Fig. 7 and Tab. 1). Before 2017, the onshore migration rates remained stable in the long term despite the large short-term fluctuations between –10~60 m/year. However, after 2017, the onshore migration rates increased significantly especially on the transects F1–2.

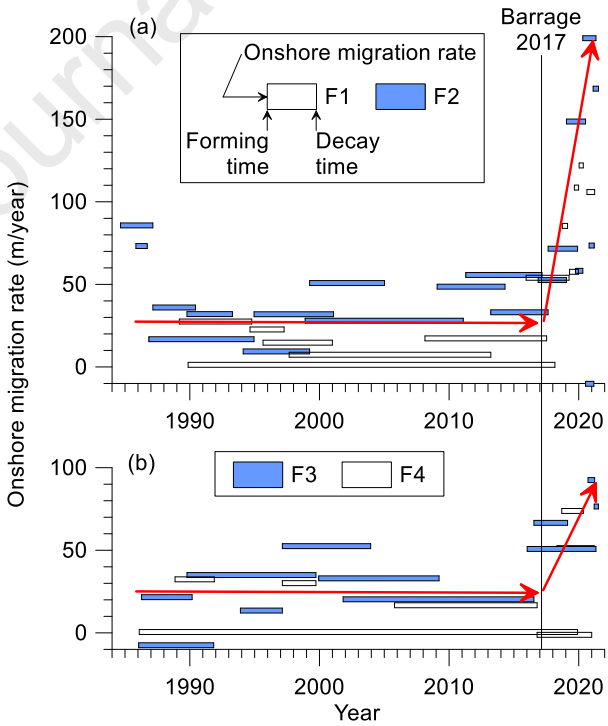

Fig. 7 Onshore migration rates of the IBSs around the Feng River mouth on the transects F1–2 (a) and F3–4 (b).

Tab. 1 Onshore migration rates of the IBSs around the Feng River mouth and their errors.

IBS and its evolution period	Starting time	End time	Forming elevation (m)	Decay elevation (m)	Data count	Onshore migration rate (m/year)	R^2	Absolute error (m/year)	Relative error
F1*0	1989/11/13	2018/3/2	–2.60	–2.46	22	1.3	0.46	0.31	24%
F1*1	1989/3/10	1994/10/10	–2.25	0.56	10	27.5	0.94	2.46	9%
F1*2	1994/8/23	1997/4/9	–1.53	–0.24	11	22.7	0.93	2.08	9%
F1*3	1995/8/26	2000/12/29	–1.75	–0.26	7	14.7	0.97	1.16	8%
F1*4	1997/8/31	2013/3/20	–2.05	0.15	10	7.4	0.97	0.46	6%
F1*5	2008/2/19	2017/7/11	–2.38	0.65	17	17.3	0.97	0.79	5%
F1*6	2015/12/9	2019/4/2	–2.44	0.41	40	54	0.96	1.79	3%
F1*7	2019/4/17	2019/12/23	–0.45	0.58	11	57.6	0.89	6.75	12%
F1*8	2018/9/26	2019/2/21	–2.45	–2.20	10	85.4	0.86	12.18	14%
F1*9	2019/8/30	2019/12/28	–2.35	–1.90	9	108.6	0.82	19.23	18%
F1*10	2020/1/12	2020/5/6	–2.28	–1.96	8	122	0.62	38.99	32%
F1*11	2020/8/19	2021/3/26	–2.31	/	14	105.9	0.93	8.39	8%
F2*1	1985/11/2	1986/9/18	0.17	1.13	4	73.2	0.99	5.20	7%
F2*2*1	1984/8/27	1987/2/25	–1.61	/	15	85.7	0.89	8.36	10%
F2*2*2	1987/2/25	1990/6/9	/	1.61	35	36	0.85	2.63	7%
F2*3	1989/10/12	1993/4/14	–0.02	1.57	24	32	0.92	2.01	6%
F2*4*1	1986/11/5	1994/12/13	–1.69	/	28	16.8	0.87	1.27	8%
F2*4*2	1994/12/13	2001/1/30	/	1.71	17	31.9	0.99	0.83	3%
F2*5*1	1994/2/12	1999/3/30	–1.71	/	6	9.4	0.80	2.35	25%
F2*5*2	1999/3/30	2005/1/9	/	2.00	28	50.8	0.99	1.00	2%
F2*6	1998/11/22	2011/2/3	–1.60	0.91	63	28	0.96	0.73	3%
F2*7	2009/1/28	2014/4/24	–1.60	1.70	15	48.6	0.96	2.75	6%
F2*8	2011/4/16	2017/3/3	–1.68	2.10	29	55.7	0.99	1.08	2%
F2*9*1	2013/3/20	2017/8/22	–1.69	/	83	33.1	0.86	1.48	4%
F2*9*2	2017/8/22	2019/11/28	/	1.24	44	71.6	0.94	2.79	4%
F2*10*1	2016/11/13	2019/1/22	–1.75	/	55	52.6	0.91	2.27	4%
F2*10*2	2019/1/22	2020/7/10	/	/	51	148.6	0.98	3.03	2%
F2*10*3	2020/7/10	2021/3/2	/	1.76	15	–10.2	0.38	3.61	35%
F2*11*1	2019/9/29	2020/4/26	–1.63	/	21	58.2	0.79	6.88	12%
F2*11*2	2020/4/26	2021/5/1	/	/	32	199.07	0.96	7.42	4%
F2*12	2020/10/18	2021/3/12	–1.74	/	7	73.5	0.88	12.14	17%
F2*13	2021/2/10	2021/7/10	–1.45	/	4	168.5	1.00	4.46	3%
F3*0	1986/1/21	1991/11/3	–1.66	–1.66	33	–7.5	0.48	1.40	19%
F3*1	1986/4/11	1990/3/5	–0.92	/	20	21.6	0.68	3.49	16%
F3*2	1989/10/12	1999/9/22	–1.62	1.09	24	35	0.99	0.75	2%
F3*3*1	1993/11/24	1997/2/20	–1.65	/	18	13.5	0.25	5.85	43%
F3*3*2	1997/2/20	2003/12/14	/	0.48	55	52.5	0.95	1.65	3%
F3*4	1999/12/11	2009/3/25	–1.67	–0.40	29	33	0.95	1.46	4%

F3*5*1	2001/10/29	2016/7/16	–1.60	/	118	20.3	0.90	0.63	3%
F3*5*2	2016/7/16	2019/2/21	/	0.58	81	66.6	0.96	1.53	2%
F3*6	2018/4/27	2021/3/12	–0.46	0.97	58	51.3	0.91	2.16	4%
F3*7	2021/3/10	2021/7/10	0.23	/	7	76.5	0.86	13.80	18%
F3*8	2016/1/8	2021/5/1	–1.65	/	127	50.8	0.96	0.93	2%
F3*9	2020/9/18	2021/3/26	–1.49	/	11	92.5	0.80	15.42	17%
F4*0	1986/2/6	2019/11/28	–2.20	–2.23	20	0.5	0.06	0.47	93%
F4*1	1988/11/10	1991/11/19	–2.26	–1.93	5	32.4	0.99	1.88	6%
F4*2	1997/2/20	1999/9/22	–2.27	–1.99	11	30.1	0.91	3.16	10%
F4*3*1	2005/10/16	2016/10/14	–2.25	/	22	16.7	0.95	0.86	5%
F4*3*2	2016/10/14	2021/1/1	/	0.03	18	–1.2	0.95	0.07	6%
F4*4	2018/9/9	2020/5/11	–2.07	–0.38	13	73.8	0.99	2.24	3%

In the first column, the number before the first "*" indicates the sequence number of the transects shown in Fig. 1, the number immediately after the first "*" indicates the sequence number of the IBSs shown in Fig. 6, and the number after the second "*" indicates the different migration periods of the IBSs shown by the red straight lines in Fig. 6. In the fourth and fifth columns, the forming and decay elevations are relevant to the mean sea level.

4.2. Forming and decay elevations of the IBSs

Fig. 8 shows the profile shapes of the transects F1–4 recently measured using RTK-GPS, and the profile shapes fit well with second-order polynomial functions. Fig. 8 also shows the satellite-derived data within one year of the RTK-GPS survey. The satellite-derived dry/wet line and waterline positions scatter around the profile shapes, which are the combined effects of the beach evolution, water level error, and image recognition error. The satellite-derived dividing line positions moved onshore along the best-fit lines and gradually arrived at the measured positions of the dividing lines.

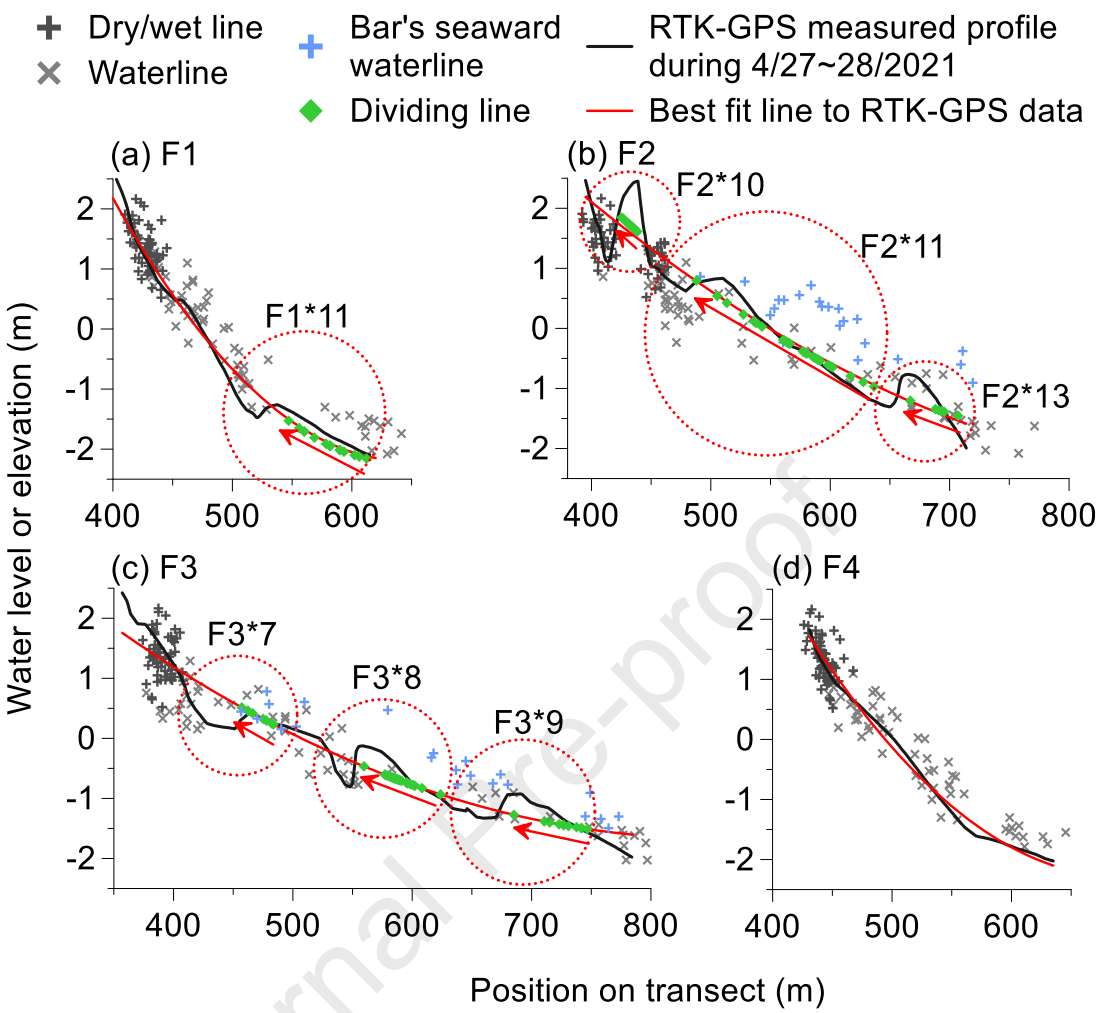

Fig. 8 Field-survey profile shapes, the satellite-derived shoreline positions of beach, and the satellite-derived positions of the IBSs on transects F1 (a), F2 (b), F3 (c), and F4 (d) around the Feng River mouth. The satellite-derived data are within one year of the RTK-GPS survey.

According to the first and last positions of the satellite-derived dividing lines (Fig. 6) and the best-fit functions of the beach profile shapes (Fig. 8), the forming and decay elevations of the IBSs were derived (Tab. 1), and their frequency distributions were calculated at the interval of 0.5 m (Fig. 9). The distribution of the forming elevation is significantly negative biased with the peak elevation located at –1.7 m and 62% of the data located in the range of –2.5~–1.5 m (Fig. 9a). However, the decay elevations are distributed in the entire intertidal zone with no obvious bias (Fig. 9b).

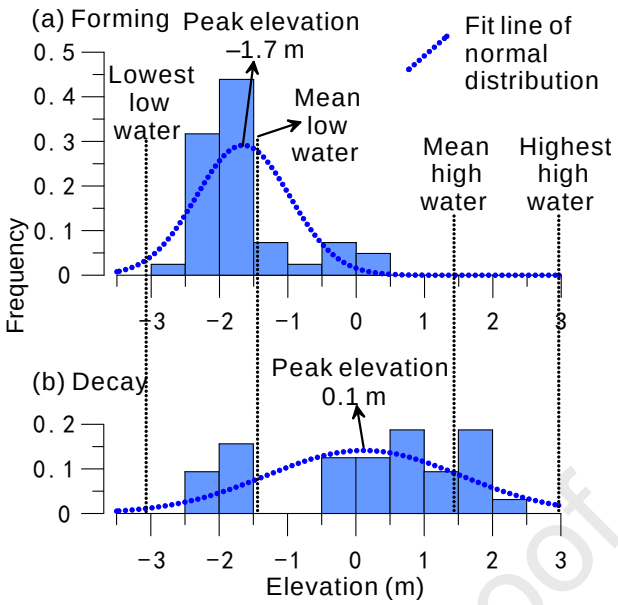

Fig. 9 Frequency distributions of the forming (a) and decay (b) elevations of the IBSs around the Feng River mouth

4.3. Planar shape changes of four typical IBSs

Four typical IBSs, each for a transect, were selected to show their planar shape changes (Fig. 10). The outlines of bars were depicted on the satellite images at the time interval of a year. When the bar images were scarce, the outlines of troughs and breakers were also depicted on the satellite images. The four typical IBSs mainly migrated onshore along the transects, while their alongshore migrations were less obvious. The bar sizes gradually decreased when they migrated onshore, and the size decrease of F3*8 was the most significant.

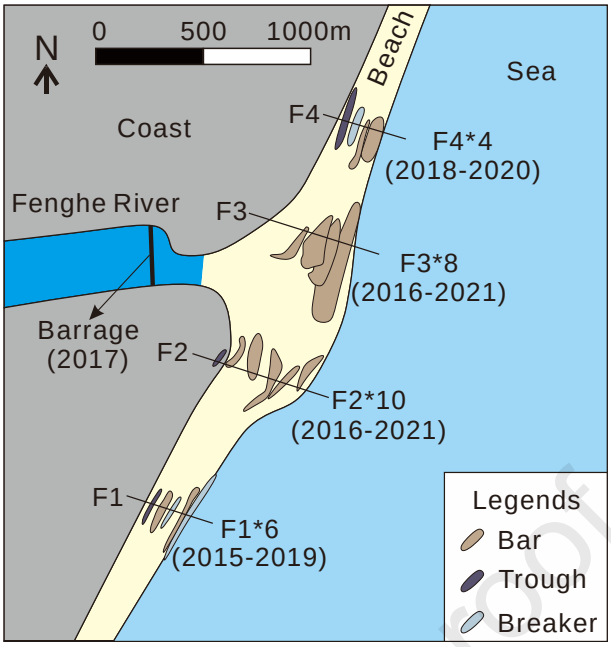

Fig. 10 Planar shape changes of four typical IBSs around the Feng River mouth. The base map was depicted from the Sentinel image of 2021/3/12 (Supplemental Fig. 1)

4.4. Error assessment results

Tab. 2 Systematic error of the satellite-derived dividing line position of the IBSs around the Feng River mouth (m)

	F1*11	F2*10	F2*11	F2*13	F3*7	F3*8	F3*9	F4	Average
RTK-GPS measured trough bottom position	521	413	479	650	451	548	660	/	532
RTK-GPS measured bar crest position	537	439	510	666	465	558	682	/	551
RTK-GPS measured dividing line position	529	426	495	658	458	553	671	/	541
Satellite-derived dividing line position	538	432	490	669	463	560	677	/	547
Systematic error of satellite-derived dividing line position	8.5	5.8	–4.9	11.0	5.1	7.1	6.1	/	5.5
RTK-GPS measured mean high water position	422	446	446	446	395	395	395	439	423

Satellite-derived mean high water position	432	455	455	455	398	398	398	443	429
Systematic error of satellite-derived mean high water position	9.8	8.8	8.8	8.8	3.0	3.0	3.0	3.6	6.5

The averages of the RTK-GPS measured bar crest and trough bottom positions were used to indicate the RTK-GPS measured dividing line positions (Tab. 2). The satellite-derived dividing line positions closest to the survey time were used to compare with the RTK-GPS measured values after they were corrected according to the onshore migration rates shown in Tab. 1. The systematic errors of the satellite-derived dividing line positions varied between –4.9~11.0 m with an average of 5.5 m. The systematic error of the satellite-derived dividing line position might originate from the registration process of the satellite images, as the systematic error of the satellite-derived high water position is 6.5 m and equivalent to the systematic error of the satellite-derived dividing line position (Tab. 2).

Tab. 3 Systematic and random errors of the dividing line positions recognized by trough, bar, and breaker methods

	Trough	Bar	Breaker	In total
Data count	623	597	186	1406
Data acquisition ratio	76%	73%	23%	172%
Systematic error (m)	–1.9	1.4	4.3	/
Random error (m)	14.0	14.8	19.3	15.3

The systematic and random errors of the dividing line positions recognized by trough, bar, and breaker methods were analyzed, respectively (Tab. 3). Relative to the total satellite image count of 816, the total acquisition ratio of the dividing line positions is greater than 100% (Tab. 3), which is owing to multiple IBSs can be perceived on a satellite image. The data counts and data acquisition ratios of the trough and bar methods are equivalent and significantly higher than that of the breaker method. The systematic and random errors are –1.9~4.3 m and 14.0~19.3 m, respectively, in which the error of the breaker method is the biggest. The random errors of the satellite-derived dividing line position (Tab. 3) are equivalent to the distances between the bar crest and trough bottom (Tab. 2) because theoretically, the dividing line can move between the bar crest and trough bottom under the effects of tide and waves.

The absolute error of the onshore migration rate varies between 0.1–39 m/year with 88% less than 8.4 m/year, and the average of the lower 88% is 2.6 m/year (Tab. 1). The relative error of the onshore migration rate varies between 2%–93% with 88% less than 18%, and the average of the lower 88% is 7%. The large errors of the remaining 12% are mainly related to the small data count used to perform the regression analysis (Fig. 11a, c; Tab. 1).

The absolute error increases with the onshore migration rate according to a second-order polynomial formula (Fig. 11b). The relative error is inversely proportional to the onshore migration rate when the onshore migration rate is less than 40 m/year (Fig. 11d), which is normal according to its calculation method. However, when the onshore migration rate is greater than 40 m/year, the relative error increases with the onshore migration rate (Fig. 11d). The abnormal phenomenon should be attributed to the roughly fixed number of satellite images available over a period (Fig. 2b), which will result in the IBSs with large onshore migration rates having less satellite-derived data, further leading to the increase of the absolute and relative errors.

The right three outliers in Fig. 11b, d indicate the data of the IBSs F2*10*2, F2*11*2, and F2*13 during 2019–2021 (Fig. 6b) when the good satellite images are 60–70 per year (Fig. 2b). The launch and operation of the Sentinel satellites significantly increased the availability of free satellite imagery, and the usage of a large number of satellite images greatly reduced the errors of the satellite-derived onshore migration rate. In the early period when the good images are about 10–20 per year (Fig. 2b), the satellite-derived onshore migration rates less than 60 m/year have small absolute error (Fig. 11b), and the satellite-derived onshore migration rates between 30–60 m/year have small relative error (Fig. 11d).

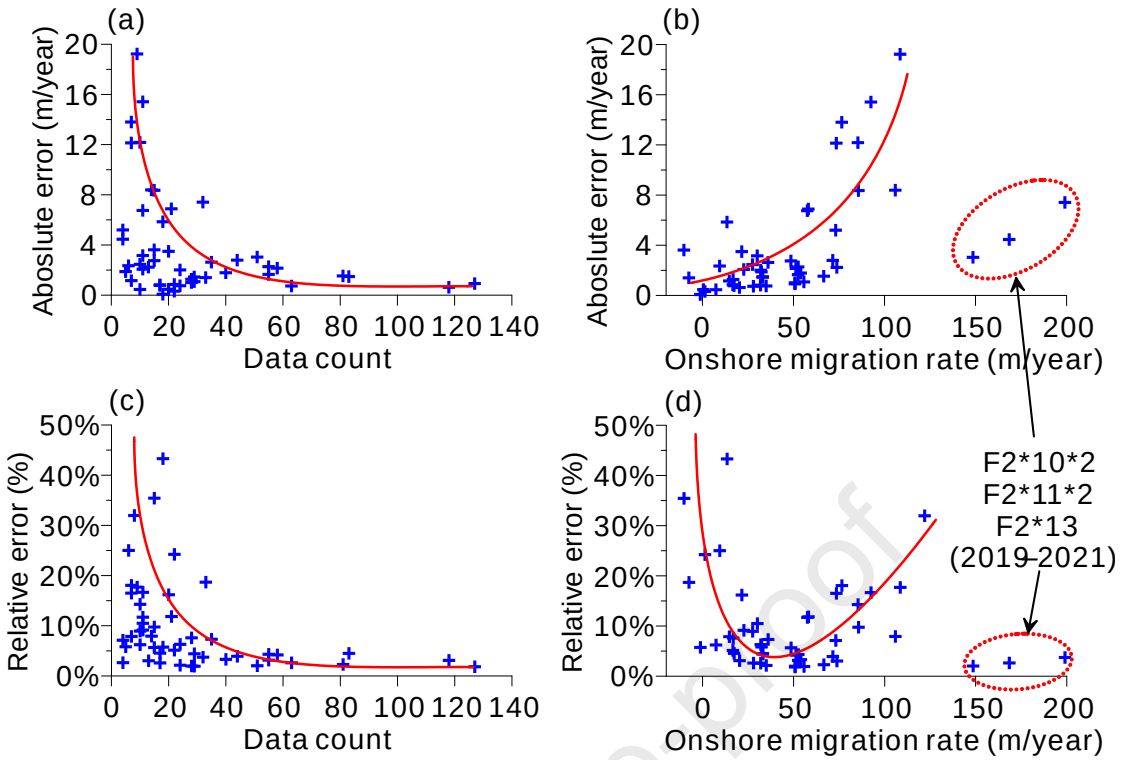

Fig. 11 Error analysis of the satellite-derived onshore migration rate of IBSs: (a) absolute error versus data count, (b) absolute error versus onshore migration rate, (c) relative error versus data count, and (d) relative error versus onshore migration rate.

5. Discussion

5.1. Comparison with previous approaches

Compared with the field survey approach, the satellite approach has an obvious deficiency in data accuracy (Fig. 8). However, the satellite approach eliminates the need for manual field surveys and can use the satellite imagery which can be downloaded freely to perform the long-term (recent decades) IBS evolution studies on most beaches in the world.

Different from previous satellite approaches, which mainly calculate the vertical elevations, the satellite approach directly recognizes the planar positions of IBSs. Previous satellite approaches commonly have complex calculation processes, need to set site-specific parameters, and need to use the satellite images under specific weather, wave, and water conditions. In contrast, the satellite approach is easy to use and has low

requirements for satellite images. The satellite images can be used as long as the beach can be perceived. Using satellite images as many as possible can not only obtain the long-term and fine time-resolution results but also further reduce the error using the statistical method.

Compared with the Argus approach, the satellite approach has an obvious deficiency in the time resolution of data. The relatively low time-resolution of satellite images restricts the ability of the satellite approach to study the evolution of IBSs with fast migration rates (Fig. 11), that's why we use as many satellite images as possible to recognize the position of IBSs. The previous Argus approaches commonly use time-averaged images to recognize the position of IBSs. The time-averaged images strengthen the central zone of the breaker but blur the boundary line of the breaker, and existing studies have shown that the central position of breaker on time-averaged Argus image is 10–20 m seaward biased relative to the bar crest position (Lippmann and Holman,1990; Ribas et al., 2010). The satellite approach not only uses the breaker images when the IBSs are submerged but also directly uses the bar and trough images when the IBSs are exposed to recognize the dividing line, and the results derived by the bar and trough methods are more reliable (Tab. 3). The systematic error of the satellite approach is 5.5 m and lower than that of the Argus approach, and the random error of the satellite approach is 15.3 m and equivalent to that of the Argus approach (Lippmann and Holman,1990; Ribas et al., 2010). The use of multiple recognition methods and as many satellite images as possible make the results obtained by the satellite approach comparable in detail and accuracy to those obtained by the Argus approach.

5.2. Evolution of the IBSs around the Feng River mouth

Regarding the forming or genesis of the IBSs around the Feng River mouth, the results show that their forming elevations were mainly distributed in the zone between the lowest low water and mean low water (Fig. 9a). This indicates that the IBSs around the Feng River mouth mainly originated from the lower part of the beach.

Different from the offshore migration of IBSs in high-energy wave conditions, such as

the coast of Australia, Japan, and the United States (e.g., Kuriyama et al., 2008; Cohn and Ruggiero, 2016; Phillips et al., 2017), the IBSs around the Feng River mouth mainly migrated onshore, which should be due to the local strong tide but weak wave condition. The occasional phenomenon of bar reset shown in Fig. 6 should be attributed to the damaging effect of the extra-strong waves (Quartel et al., 2007).

After their decay, approximately 1/4 of the disappeared IBSs would continue to move onshore as troughs and affect the dry/wet line positions of the local beach (Fig. 6). However, the onshore migration of the dry/wet line position triggered by the decay of IBS seems to have little influence on the long-term evolution of the beach as the dry/wet line position migrated back subsequently. Incidentally, the significant shoreline retreat of ~150 m after the decay of IBS F3*1 should be mainly caused by artificial sand mining (Fig. 6c).

Regarding the alongshore distribution of the IBSs, the IBS count on the southern transects F1–2 was twice of that on the northern transects F3–4 (Fig. 6), which might be attributed to the dominant sediment transport direction in the study area is from north to south (Cui and Li, 1987), and therefore the sands trapped by the river mouth were mainly transported southward. The IBS count on the transects F2–3 was higher than that on the transects F1 and F4 (Fig. 6), which should be attributed to the transects F2–3 being closer to the river mouth.

In the cross-shore direction, although there is an intuitive finding of the acceleration of the onshore migration (Fig. 6), the statistical analysis results did not show any correlation between the onshore migration rates and the elevations. Further study found that the accelerated onshore migration of IBS generally occurred when a new IBS was formed on its outside, such as the F2*5 and F2*6, F3*5 and F3*8 (Fig. 6b and c), which indicates that the existence of outer IBSs can reduce the wave energy acting on the inner IBSs (Short and Aagaard, 1993; Wijnberg and Kroon, 2002), and in turn accelerate the onshore migration of the inner IBSs under the joint action of waves and tides. The above further implies that the effect of waves on the migration of IBSs is not a monotonic function with wave energy, and perhaps the waves with moderate energy are more favorable for the onshore migration of IBSs.

Regarding the temporal change of the IBSs, the sharp acceleration of the onshore migration after 2017 (Fig. 7) should be mainly related to the construction of the barrage just 400 m to the river mouth in 2017 (Fig. 1). Before the barrage was built, the flood currents adjacent to the southwestern bank (transects F1–2) of the river mouth should be slower than that of the nearshore because of the large tidal prism of the wide river channel (Fig. 1). For the same reason, the ebb currents adjacent to the northeastern bank (transects F3–4) of the river mouth should be quicker. The above speculations were confirmed by the numerical simulation results of Kuang et al. (2019b). The barrage built in 2017 could block the inflow of flooding water into the river channel, therefore enhancing the flood currents on the southwest bank of the river mouth and accelerating the onshore migration of the IBSs on transects F1–2. Similarly, the construction could also decrease the outflow of ebb water from the river channel, therefore weakening the ebb currents on the northeast bank of the river mouth, and in turn, accelerating the onshore migration of the IBSs on transects F3–4. The acceleration effect on transects F1–2 was caused by the strengthening of flood currents, which was active; while the acceleration effect on transects F3–4 was caused by the weakening of ebb currents, which was passive. This might be the reason why the acceleration effect on transects F1–2 was stronger than that on transects F3–4 (Fig. 7).

The onshore migration of the IBSs should exact a positive influence on the evolution of surrounding beaches because they provided a sand supply. However, although many IBSs have migrated onshore, the beach evolution has remained stable (Fig. 6), which might be attributed to the negative impacts of other factors. The sea level along the coast of China was rising at 3.4 mm/year during 1980–2020 (China Sea Level Bulletin 2020, http://www.mnr.gov.cn/), and combined with the Feng River no longer discharged sand into the sea, the Lingnan Beach commonly experienced erosion (Cui and Li, 1987; Yang et al., 2005). The onshore migration of many IBSs offset the negative impact of the above two factors, causing the evolution of beaches around the river mouth to remain stable. The beach near the transect F2 experienced a slight accretion after 2017 (Fig. 6b), which should be attributed to the significantly accelerated onshore migration of IBSs on transect

F2 due to the barrage construction mentioned above.

Under the circumstance of the Feng River no longer discharged sand into the sea, the count of the newly-formed IBSs around the river mouth did not show decreasing trends, which indicates that the river-discharged sediment is not essential to the formation of new estuarine IBSs. River mouth or delta can capture the sediment transported alongshore and cross-shore by interfering with the water flow with its unique topography and geomorphology (Harrison, 2015), resulting in the continuous formation of estuarine IBSs.

6. Conclusions

This paper provides a new approach for studying the evolution of IBSs based on free satellite imagery, and the satellite approach can be used to study the long-term evolution of IBSs on almost all beaches in the world. This will greatly expand the study object pool and facilitate the selection of study objects in different marine conditions (weak and strong waves; micro-, meso-, and macro-tidal ranges) to have a comprehensive understanding of the evolution of IBSs, contributing to the establishment of general models in the future.

This satellite approach adopts three methods, namely trough, bar, and breaker methods, to recognize the planar positions of IBSs at low, middle, and high water levels, respectively. Therefore, the approach can use satellite images at any historical water level. The systematic and random errors of the satellite-derived dividing line positions are 5.5 and 15.3 m, respectively, comparable to the results based on time-averaged Argus images, which generally have fine resolution both in time and space.

This approach has low requirements on satellite images and is conducive to making full use of the precious satellite images to study the long-term evolution of IBSs at fine time resolution. Usable free satellite images of the Feng River mouth were 10–20 per year in 1984–2015 and 60–70 per year in 2018–2020. Statistical analysis of a large amount of data can improve the accuracy of research results, which is necessary for studying the highly dynamic evolution of IBSs. Except for the 12% results with large errors, the absolute and relative errors of the satellite-derived onshore migration rates are averaged 2.6 m/year and 7%, respectively.

This paper also introduces the usage of the satellite approach based on a case study of the IBSs around the Feng River mouth in China. The case study shows that the IBSs were mainly formed in the zone between the lowest low water and mean low water. After their formation, most IBSs migrated onshore under the joint influence of waves and tides, and a few IBSs can exist stably at the low water level. Different from their formation, the decay of IBSs occurred evenly in the whole intertidal zone with no obvious bias. The barrage construction just 400 m to the river mouth in 2017 seriously affected local tidal conditions and accelerated the onshore migrations of the estuarine IBSs. The historical onshore migrations of many IBSs compensated for the adverse effects of the rapid relative sea-level rise and the barrage constructions, maintaining the stability or accretion of the local beach.

Acknowledgments

This work was supported by the Shandong Provincial Natural Science Foundation, China (ZR2019MD037), the Fundamental Research Funds for the Central Universities (202072003), and the National Natural Science Foundation of China (41776059). We are greatly indebted to the Editor-in-Chief Iñigo J. Losada and two anonymous reviewers for their professional comments and valuable suggestions.

Data Availability

The software and part of the satellite images can be found at https://github.com/ouczxd/CASPRS. All the satellite images can be downloaded from Google Earth Engine (https://earthengine.google.com/) using the JavaScript program: “GEEdownloader” (https://github.com/ouczxd/CASPRS).

References

1. Aleman, N., Certain, R., Robin, N., Barusseau, J. P. 2017. Morphodynamics of slightly oblique nearshore bars and their relationship with the cycle of net offshore migration.

Marine Geology, 392, 41–52.

2. Alexandrakis, G., Manasakis, C., Kampanis, N.A., 2015. Valuating the effects of beach erosion to tourism revenue. A management perspective. Ocean & Coastal Management, 111:1–11.
3. Anthony, E.J., Levoy, F., Monfort, O., Degryse-Kulkarni, C. 2005. Short-term intertidal bar mobility on a ridge-and-runnel beach, Merlimont, northern France. Earth Surface Processes and Landforms, 30: 81–93.
4. Bergsma, E.W.J., Almar, R., Maisongrande, P. 2019. Radon-augmented Sentinel-2 satellite imagery to derive wave-patterns and regional bathymetry. Remote Sensing, 11, 1918.
5. Bian, S., Liu, J., Zhang, Z., Liu, L., Hu, Z. 2019. Risk and the dynamic mechanism of the beach close to the tidal Inlets. Ocean Development and Management, 2: 80-85 (In Chinese with English abstract).
6. Biausque, M., Grottoli, E., Jackson, D.W.T., Cooper, J.A.G. 2020. Multiple intertidal bars on beaches: A review. Earth-Science Reviews, 210,103358.
7. Bouvier, C., Balouin, Y., Castelle, B. 2017. Video monitoring of sandbar-shoreline response to an offshore submerged structure at a microtidal beach. Geomorphology, 295: 297–305.
8. Caldwell, N., Houser, C., Meyer-Arendt, K. 2013. Ability of beach users to identify rip currents at Pensacola Beach, Florida. Natural Hazards, 68(2), 1041–1056.
9. Cheng, J., Wang, P. 2018. Dynamic equilibrium of sandbar position and height along a low wave energy micro-tidal coast. Continental Shelf Research, 165: 120–136.
10. Cohn, N., Ruggiero, P. 2016. The influence of seasonal to interannual nearshore profile variability on extreme water levels: modeling wave runup on dissipative beaches. Coastal Engineering, 115: 79–92.
11. Cui, C.Q., Li, J.F. 1987. The coastal geomorphological steps and types of Lingshan Bay and its neighbour regions of Shandong Province. Transactions of Oceanology and Limnology, 3: 47–51 (In Chinese with English abstract).
12. Cui, J.R., Xia, D.X. 1992. The relationship between coastal morphology and the

characteristics of waves and tides of Shandong Peninsula. Journal of Oceanography of Huanghai & Bohai Seas, 10(3): 20–25 (In Chinese with English abstract).

13. Di Leonardo, D., Ruggiero. P. 2015. Regional scale sandbar variability: observations from the U.S. pacific northwest. Continental Shelf Research, 95, 74–88.
14. Fernández-Mora, A., Calvete, D., Falqués, A., de Swart, H. E. 2015. Onshore sandbar migration in the surf zone: New insights into the wave-induced sediment transport mechanisms. Geophysical Research Letters, 42, 2869–2877, doi:10.1002/2014GL063004.
15. Gijsman, R., Visscher, J., Schlurmann, T. 2019. The lifetime of shoreface nourishments in fields with nearshore sandbar migration. Coastal Engineering, 152, 103521.
16. Guedes, R.M.C., Bryan, K.R., Coco, G., Holman, R.A., 2011a. The effect of tides on swash statistics on an intermediate beach. Journal of Geophysical Research Oceans, 116, C04008, doi:10.1029/2010JC006660.
17. Guedes, R.M.C., Calliari, L.J., Holland, K.T., Plant, N.G., Pereira, P.S., Alves, F.N.A. 2011b. Short-term sandbar variability based on video imagery: Comparison between Time–Average and Time–Variance techniques. Marine Geology, 289: 122–134.
18. Harrison, S.R. 2015. Morphodynamics of Ebb-Tidal Deltas (Thesis, Doctor of Philosophy (PhD)). University of Waikato, Hamilton, New Zealand. Retrieved from https://hdl.handle.net/10289/9810.
19. Harrison, S.R., Bryan, K.R., Mullarney, J.C. 2017. Observations of morphological change at an ebb-tidal delta. Marine Geology, 385: 131–145.
20. Hayes, M.O., 1979. Barrier island morphology as a function of tidal and wave regime. In: S.P. Leatherman (Ed.), Barrier Islands: From the Gulf of St. Lawrence to the Gulf of Mexico. Academic Press, New York, USA, pp. 1– 28.
21. Hoefel, F., Elgar, S. 2003. Wave-induced sediment transport and sandbar migration. Science, 299: 1885–1887.
22. Holman, R.A., Stanley, J. 2007. The history and technical capabilities of Argus. Coastal Engineering, 54(6–7), 477–491.

23. Holman, R., Plant, N., Holland, T. 2013. Cbathy: a robust algorithm for estimating nearshore bathymetry. Journal of Geophysical Research Oceans, 118, 2595–2609, doi:10.1002/jgrc.20199.

24. Jackson, N.L., Nordstrom, K.F., 2020. Trends in research on beaches and dunes on sandy shores, 1969–2019. Geomorphology, 366, 106737. https://doi.org/10.1016/j.geomorph.2019.04.009.

25. King, C.A.M., Williams, W.E., 1949. The formation and movement of sand bars by wave action. The Geographical Journal, 113, 70–85.

26. Kroon, A., Masselink, G. 2002. Morphodynamics of intertidal bar morphology on a macrotidal beach under low-energy wave conditions, North Lincolnshire, England. Marine Geology, 190, 573–591.

27. Kuang, C., Mao, X., Gu, J., Niu, H., Ma, Y., Yang, Y., Qiu, R., Zhang, J. 2019a. Morphological processes of two artificial submerged shore-parallel sandbars for beach nourishment in a nearshore zone. Ocean & coastal management, 179, 104870.

28. Kuang, C., Zhao, F., Gu, J., Tang, L. 2019b. Scouring and silting characteristics and bed evolution mechanism in narrow Small Estuary. Journal of the Tongji University (Natural Science), 47(10): 1437–1445 (In Chinese with English abstract).

29. Kuriyama, Y., Ito, Y., Yanagishima, S., 2008. Medium-term variations of bar properties and their linkages with environmental factors at Hasaki, Japan. Marine Geology, 248 (1–2), 1–10.

30. Lafon, V., De Melo Apoluceno, D., Dupuis, H., Michel, D., Howa, H., Froidefond, J.M. 2004. Morphodynamics of nearshore rhythmic sandbars in a mixed-energy environment (SW France): I. Mapping beach changes using visible satellite imagery. Estuarine, Coastal and Shelf Science, 61(2), 289–299.

31. Lippmann, T.C., Holman, R.A., 1990. The spatial and temporal variability of sand bar morphology. Journal of Geophysical Research Oceans, 95, 11575–11590.

32. Luijendijk, A., Hagenaars, G., Ranasinghe, R., et al., 2018. The State of the World's Beaches. Scientific Reports, 8:6641. DOI:10.1038/s41598-018-24630-6.

33. Masselink, G., Anthony, E.J., 2001. Location and height of intertidal bars on macrotidal

ridge and runnel beaches. Earth Surface Processes and Landforms, 26 (7), 759–774. https://doi.org/10.1002/esp.220.

34. Masselink, G. 2004. Formation and evolution of multiple intertidal bars on macrotidal beaches: application of a morphodynamic model. Coastal Engineering, 51(8/9), 713–730.
35. Masselink, G., Kroon, A., Davidson-Arnott, R.G.D. 2006. Morphodynamics of intertidal bars in wave-dominated coastal settings — A review. Geomorphology, 73: 33–49.
36. Matsumoto, K., Takanezawa, T., Ooe, M., 2000. Ocean tide model developed by assimilating TOPEX/POSEIDON altimetry data into hydrodynamical model: a global and a regional model around Japan. Journal of Oceanography, 56, 567–581.
37. Miles, A., Ilic, S., Whyatt, D., James, M.R., 2019. Characterizing beach IBSs using multi-annual LiDAR data. Earth Surface Processes and Landforms, 44 (8), 1572–1583.
38. Moore, L.J., Sullivan, C., Aubrey, D.G. 2003. Interannual evolution of multiple longshore sand bars in a mesotidal environment, Truro, Massachusetts, USA. Marine Geology, 196 (3–4), 127–144.
39. Najar, M. A., Thoumyre, G., Bergsma, E., Almar, R., Benshila, R., Wilson, D. G. 2021. Satellite derived bathymetry using deep learning. Machine Learning, https://doi.org/10.1007/s10994-021-05977-w.
40. Nicholls, R.J., Cazenave, A. 2010. Sea-level rise and its impact on coastal zones. Science, 328(5985):1517–20.
41. Phillips, M. S., Harley, M.D., Turner, I.L., Splinter, K.D., Cox, R.J. 2017. Shoreline recovery on wave-dominated sandy coastlines: the role of sandbar morphodynamics and nearshore wave parameters. Marine Geology, 385, 146–159.
42. Quartel, S., Ruessink, B.G. and Kroon, A., 2007. Daily to seasonal cross-shore behavior of quasi-persistent intertidal beach morphology. Earth Surface Processes and Landforms 32, 1293–1307.
43. Quartel, S., Kroon, A., Ruessink, B.G. 2008. Seasonal accretion and erosion patterns of a microtidal sandy beach. Marine Geology, 250, 19–33.
44. Radermacher, M., De Schipper, M.A., Price, T.D., Huisman, B., Aarninkhof, S., Reniers,

A. 2018. Behaviour of subtidal sandbars in response to nourishments. Geomorphology, 313: 1–12.

45. Reichmüth, B., Anthony, E.J. 2007. Tidal influence on the intertidal bar morphology of two contrasting macrotidal beaches. Geomorphology, 90(1–2), 101–114.
46. Ribas, F., Ojeda, E., Price, T.D., Guillén, J. 2010. Assessing the suitability of video imaging for studying the dynamics of nearshore sandbars in tideless beaches. IEEE Transactions on Geoscience and Remote Sensing, 48(6), 2482–2497.
47. Román-Rivera, M.A., Ellis, J.T. 2019. A synthetic review of remote sensing applications to detect nearshore bars. Marine Geology, 408: 144–153.
48. Sassa, S., Watabe, Y. 2009. Persistent sand bars explained by geodynamic effects, Geophysical Research Letters, 36, L01404, doi:10.1029/2008GL036230.
49. Scott, T. M., Russell, P. E., Masselink, G., Austin, M. J., Wills, S., Wooler, A. 2011. Rip current hazards on large-tidal beaches in the United Kingdom. New York: CRC Press.
50. Short, A.D., Aagaard, T., 1993. Single- and multi-bar beach change models. Journal of Coastal Research, SI 15, 141–157.
51. Stive, M.J.F., ReniersElgar, A.J.H.M. 2003. Sandbars in motion. Science, 299: 1855–1856.
52. van de Lageweg, W.I., Bryan, K.R., Coco, G., Ruessink, B.G. 2013. Observations of shoreline–sandbar coupling on an embayed beach. Marine Geology, 344: 101–114.
53. van Dongeren, A., Plant, N., Cohen, A., Roelvink, D., Haller, M.C., Catalan, P. 2008. Beach wizard: nearshore bathymetry estimation through assimilation of model computations and remote observations. Coastal Engineering, 55(12), 1016–1027.
54. van Enckevort, I.M.J., Ruessink, B.G. 2001. Effect of hydrodynamics and bathymetry on video estimates of nearshore sandbar position. Journal of Geophysical Research Oceans, 106(C8), 16969–16979.
55. van Houwelingen, S., Masselink, G., Bullard, J., 2006. Characteristics and dynamics of multiple intertidal bars, north Lincolnshire, England. Earth Surface Processes and Landforms, 31, 428–443.
56. Vousdoukas, M.I., Ranasinghe, R., Mentaschi, L., Plomaritis, T. A., Athanasiou, P.,

Luijendijk, A., Feyen, L. 2020. Sandy coastlines under threat of erosion. Nature Climate Change, 10:260–263. https://doi.org/10.1038/s41558-020-0697-0.

57. Wijnberg, K.M., Kroon., A., 2002. Barred beaches. Geomorphology, 48:103–120.
58. Wright, L.D., Short, A.D., 1984. Morphodynamic variability of surf zones and beaches: a synthesis. Marine Geology, 56, 93–118.
59. Xu, F.J., Zhao, Y.F., Li, C.S., Sun, G.Y., Zhang, K., Tian, X., Wang, X.Y. 2014. Characteristics of sediment distribution and influencing factors at the Lingshanwan bathing beach of Qingdao. Marine Science Bulletin, 33(2): 157–162 (In Chinese with English abstract).
60. Yang, M., Xia, D.X., Gu, D.Q., Xue, Z., Feng, A.P. 2005 Geographic Environmental Evolution in the Qingdao Coastal Area Under the Influence of Global Change. Advances in Marine Science, 23(03): 45–52 (In Chinese with English abstract).
61. Zhang, X.D., Yang, Z.S., Zhang, Y.X., Ji, Y., Wang, H.M., Lv, K., Lu, Z.Y. 2018. Spatial and temporal shoreline changes of the southern Yellow River (Huanghe) Delta in 1976–2016. Marine Geology, 395: 188–197.
62. Zhang, X.D., Fan, D.D., Yang, Z.S., Xu, S.M., Chi, W.Q., Wang, H.M., 2020. Sustained growth of river-mouth bars in the vulnerable Changjiang Delta. Journal of Hydrology, 590, 125450. https://doi.org/10.1016/j.jhydrol.2020.125450.
63. Zhang, X.D., Tan, X.W., Hu, R.J., Zhu, L.H., Wu, C., Yang, Z.S. 2021a. Using a transect-focused approach to interpret satellite images and analyze shoreline evolution in Haiyang Beach, China. Marine Geology, 438, 106526. https://doi.org/10.1016/j.margeo.2021.106526.
64. Zhang, X.D., Xie, R., Fan, D.D., Yang, Z.S., Wang, H.M., Wu, C., Yao, Y.H. 2021b. Sustained growth of the largest uninhabited alluvial island in the Changjiang Estuary under the drastic reduction of river discharged sediment. Science China Earth Sciences, 64(10): 1687-1697. https://doi.org/10.1007/s11430-020-9746-3.

- A new satellite approach was provided to study the evolution of intertidal bar systems
- The approach uses bar, trough, and breaker methods to recognize the position of IBS
- The long-term evolution of IBSs around a river mouth was revealed and analyzed

Declaration of interests

☒ The authors declare that they have no known competing financial interests or personal relationships that could have appeared to influence the work reported in this paper.

☐The authors declare the following financial interests/personal relationships which may be considered as potential competing interests: